Applied Energy 130 (2014) 148–156

Contents lists available at ScienceDirect

Applied Energy

journal homepage: www.elsevier.com/locate/apenergy

Wave heave energy conversion using modular multistability

R.L. Harne [a,*], M.E. Schoemaker [b], B.E. Dussault [a], K.W. Wang [a]

[a] Department of Mechanical Engineering, University of Michigan, Ann Arbor, MI 48109, USA
[b] Department of Mechanical and Aerospace Engineering, University of Florida, Gainesville, FL 32611, USA

HIGHLIGHTS

- An alternative power take off concept is explored for mobile wave energy converters.
- A multistable chain is developed for kinetic energy conversion from wave heaves.
- Bistable links join the chain cells and induce impulses due to extension–compression.
- Chain modularity enhances impulsive kinetics by local–global dynamics transformation.
- Numerical and experimental data indicate strong potential for multistable chain.

ARTICLE INFO

Article history:
Received 26 November 2013
Received in revised form 10 March 2014
Accepted 20 May 2014

Keywords:
Mobile wave energy converter
Multistability
Impulsive dynamics
Electromagnetic induction

ABSTRACT

In calm sea environments and for compact architectures, the power generation performance of wave energy converters may be drastically inhibited due to undesired dissipative effects in the conversion mechanisms. This research develops an alternative power take-off methodology to surmount these challenges and to enable practical wave energy conversion for mobile converter architectures that could power monitoring instrumentation or telecommunications. Building upon related research findings and engineering insights, the basis for energy conversion is the harnessing of impulsive kinetics induced as a multistable structure is extended and compressed. A prototype system is built and analyzed to evaluate the potential for this conversion framework. Composed of modular "cells", the chain-like platform exhibits an increased number of stable configurations with each additional unit cell. Extension and compression of one end of the multistable chain (representative of wave heaving) while the opposing end remains mostly fixed, excites high frequency inter-cell dynamics due to impulsive transitions amongst configurations that are converted to electric current through electromagnetic induction. An experimentally validated model is utilized to gain insight towards successful realization of the power conversion concept and design guidelines are derived to maximize performance and ensure viability.

1. Introduction and motivation

The heaving motion of sea and ocean waves is one of the most persistent and dense renewable energy resources in marine environments [1,2], making it appealing to power off-shore operational bases or to supplement or replace other supplies on a continental electrical grid. Numerous power take-off (PTO) solutions have been proposed over the years [3–6], while highly dissipative PTO mechanisms based upon pneumatics or hydraulics have become common choices for wave energy converters (WECs) intended for large-scale power generation and electric grid integration [3,4].

Since pneumatic or hydraulic coupling stages are eliminated, directly driven PTO concepts based on electromagnetic induction have been developed for improved large-scale WEC efficiency. In the context of wave energy applications, direct drive "describes the direct coupling of the buoy's speed and force to the generator without the use of hydraulic fluid or air" [7]. A breadth of research has demonstrated promise in laboratory and field testing for this PTO [7–14]. The experimental systems in these studies are often physically large and massive, may require fixed mooring, and regularly deliver average powers of 10–1000 W. While this power is too low for grid integration, it is acceptable during research development.

In contrast to large-scale energy conversion, the focus of the present paper is to realize mobile WEC architectures that power self-sustaining, waterborne instrumentation or telecommunication systems. For this purpose, power generation around 1–10 W is sufficient and platforms of <100 kg mass and <10 m length are preferred for improved mobility. Many of the designs in the previously

* Corresponding author. Tel.: +1 7346158747.
E-mail address: rharne@umich.edu (R.L. Harne).

http://dx.doi.org/10.1016/j.apenergy.2014.05.038
0306-2619/

cited literature are not suited for this purpose since they are large by mass and dimension and are not easily re-deployed. Fewer investigations have focused on mobile WEC platforms for low-power applications. Portable WECs using directly driven PTO based on transmissions with rotary generators [15–17] and linear electromagnetic induction [18–21] have been recently explored. In these studies, average power generation spanning around 0.01–100 W has been demonstrated through modeling and experimentation. One trend from the studies was that prototype development exceeded 100 kg total WEC mass [16] while some full-scale systems were predicted to have mass of 500 kg [19,20]. The need for large masses is partially due to the directly driven PTO since the resistance forces are a combination of friction and high, continuous electromagnetic damping. Although damping ratios are infrequently reported for comparison to the present research, in one example damping ratios of around 0.75–1 (critically damped) were experimentally identified, collecting together viscous and friction effects [18]. For large-scale WECs, the damping forces are more readily overcome by momentum of large moving inertia [2]. Yet for lightweight and mobile WEC and considering the high variability of sea activity [22], such dissipations are difficult to surmount, particularly to break through the stall forces of friction for small actuating wave motions [23].

These challenges are the stimulus of this research towards development of an alternative PTO concept well-suited to realize mobile WECs. The following sections introduce the new PTO mechanism and present the rationales supporting the chosen design. Following experimental validation, a model of the PTO is employed to study the influences of system modularity and excitation frequency on energy conversion performance due to controlled excitation and simulated wave input. Throughout the investigations, design principles are provided for successful realization of the proposed PTO for efficient and mobile wave energy conversion.

2. PTO mechanism design

A key challenge for WEC employing directly driven rotary or linear induction PTO is the high continuous electromagnetic damping that works against the inertial mass motions (relative to a mostly fixed opposing end), which for slow velocities can lead to stalling if inertial forces do not exceed friction thresholds [23]. The PTO mechanism developed in this research alleviates this concern by combination of a modular multistable design and the use of impulsive dynamics for energy conversion.

In the field of vibration energy harvesting, the concept of energy generation using *impulsive kinetics* has received recent attention [24–27]. The objectives of these works are the development of alternative means for powering small electronics using very low frequency excitations and minimization of the excitation level required to generate power. Of particular relevance to the present study, Karami et al. [27] developed a compact, vibration energy harvester excited by impulsive interactions between dynamic piezoelectric beams and a rotating wind turbine. Because the impulsive interactions could be directly adjusted to govern the minimum actuating energy (wind speed) required to generate power, the harvester system was shown to overcome damping, friction, and low wind speed limitations of conventional directly- and gearbox-driven wind energy conversion systems. The challenges faced in development of compact wind energy converters are similar to the wave energy application of present interest. As demonstrated in the comparable wind energy application [27], a PTO based upon impulsive interactions may be a suitable alternative for compact, mobile WEC which are less able to overcome minimum actuating force and displacement requirements of direct drive PTO because of their reduced mass. Apart from the early efforts [24–27], much remains to be known about feasibility and effective adoption of impulsive kinetics for *wave energy conversion*.

The common theme of the prior studies [24–27] is the use of *bistability* to obtain the impulsive responses. Two reviews [28,29] describe numerous research efforts in the field of vibration energy harvesting with bistable systems which are largely focused on utilizing continuous switching behaviors. Within this body of work, recent findings have shown that coupling bistable elements to other dynamic bodies may greatly enhance the net energy conversion per harvester mass [30,31]. These *coupled system* studies likewise focused on continuously switching bistable dynamics which are not easily obtained for very low frequency excitations.

Following the insights described above, the aim of this work is to bring together the two promising research developments – *bistable impulsive kinetics* and *coupled dynamic systems* for energy harvesting – to realize mobile WEC platforms for low frequency and large displacement wave motions.

Fig. 1 illustrates the framework of the proposed PTO developed to integrate the two energy conversion potentials. The PTO is shown as embedded within one possible WEC architecture. The WEC is composed of a mostly submerged spar constrained in position by sufficient resistance, e.g., a submerged plate or temporary anchoring, and a buoy that moves along with the transverse wave motions. The relative displacement between spar and buoy actuates the top end of a chain of modular "cells" housed within the spar. The chain of cells connects the bottom of the spar to the actuating rigid connection. Therefore, motion between the buoy and spar extends and compresses the multi-cell chain, Fig. 1(a and b), respectively.

As illustrated by the schematic in Fig. 1(c), each unit cell is composed of two halves secured together by a threaded connection. One part of the mass is the cylinder structure and inner magnet. The remaining cell mass is the frame structure, the radial array of outer magnets, an induction coil, and the threaded connection. Two adjacent cells interact through restoring forces due to a linear spring connection and magnetic fields. The polarity orientations of the outer magnet radial array and the moving inner magnet of the adjacent cell are such that the two cells' *relative* displacements exhibit *bistability*, which leads to an energetic transition from one stable configuration to the other when the interface of two adjacent cells is extended beyond a critical point. The stable states are illustrated in Fig. 1(a and b) showing the interface between adjacent cells in the (a) extended and (b) compressed configurations. Because the cell relative displacements from extended to compressed configurations (and vice versa) involve the inner magnet passing through the induction coil of the adjacent cell and impulsively vibrating at a high natural frequency after the transition, electrical current is generated in the coil due to the switch in stable configuration. Thus, the proposed PTO is not intended to be excited as if to resonate. Instead, via the bistable interfaces, an up-conversion occurs from very low frequency actuating wave heaves to higher frequency impulsive inter-cell dynamics for energy conversion.

The PTO system adopts a modular architecture aligned with the coupled system design strategy found to enhance performance per mass of bistable energy harvesting systems [30,31]. Connecting the cells of the proposed PTO in series, as in the experimental system shown in Fig. 1(d), the activation of switching dynamics between cells transmits impulses along the chain length, transforming otherwise local behaviors into global energy conversion dynamics. The successive and cascading impulsive electrical responses from chain extension and compression are then utilized to charge energy storage elements for powering instrumentation systems. The minimum threshold of actuating force which leads to an

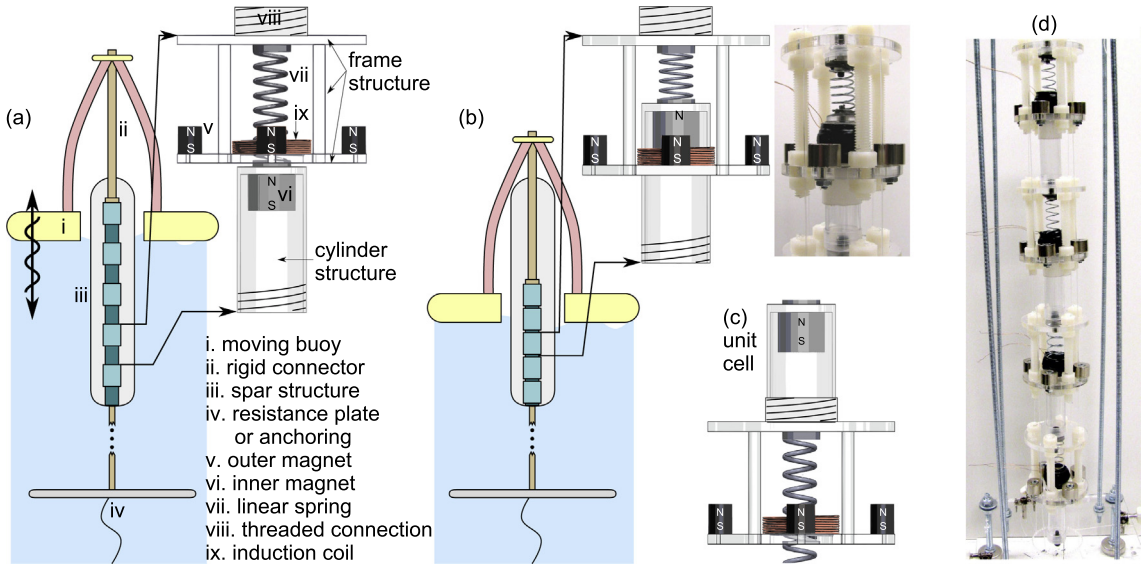

Fig. 1. Cross-section of WEC with modular multi-cell chain within spar when the chain is (a) fully extended and (b) fully compressed, showing adjacent cell interface configurations. Corresponding interface from prototype shown in compressed configuration. (c) Cross-section of unit cell assembly. (d) Prototype 4-cell chain in fully extended configuration.

impulsive switch may be readily adjusted by design. The performance trade-off is that the magnitude of actuating energy required to induce an impulse directly relates to how energetic the impulse is and, hence, how much electrical energy is generated as the inner magnet undergoes underdamped oscillations within the induction coil. However, collectively, the energy conversion benefits from highly energetic impulsive dynamics, the ability to excite impulses from much lower amplitude input motions through design of the energy barrier, and the modular architecture provide the multistable PTO chain a versatile capacity to convert electrical power from progressively smaller actuating forces and wave motions. In contrast to the friction and electromagnetic damping forces of generators or sliding armatures which may require added mass to overcome [21], the adjustable energy barriers and stable configurations of the proposed PTO enable a valuable means to ensure power generation despite small actuating motions, as described in the following section.

3. Framework of operation

A model of the PTO framework is formulated to demonstrate the essential framework of power conversion. Fig. 2(a) illustrates the modeling convention for the absolute uni-axial motions x_j of the jth unit cell of the PTO system. There are four coupling components between cell masses. From left to right in Fig. 2(a), F_j^m is the magnetic restoring force between the outer radial array and inner magnet, k_j is the linear spring constant, d_j is the damping constant representing mechanical losses in the system, and θ_j is an electromagnetic transducer constant related to the coupling strength between the inner magnet and the induction coil. The undeformed linear spring length is l_j. A scalar multiplier is defined for use in modeling magnetic interactions by $\beta_j = 1$ when the undeformed length leads to the inner magnet center of mass aligning with the midplane of the outer magnet array, the configuration specifically shown in Fig. 2(b). The configuration of $\beta_j = 1$ corresponds to the plane of unstable equilibrium generated by the magnetic interactions. Values of β greater or less than 1 represent percentage offset of the spring undeformed length that perturb the inner magnet center of mass from this plane, the purposes of which will be demonstrated in the following model evaluations. For clarity, the spring length of the unit cell assembly in Fig. 1(c) would be multiplied by scalar $\beta < 1$ since the undeformed length extends below the plane of unstable equilibrium. In the prototype, the frame structure height was adjustable so that for a given undeformed spring length, any desired offset (and hence multiplier β) could be obtained.

Profiling of the multistable PTO chain potential energy sheds light on the minimum actuation, i.e., wave motion, required to induce an impulsive response for electrical energy generation and helps to ensure bistability is exhibited between all adjacent cell pairs. The total potential energy of a cell is the summation of magnetic, spring, and gravitational effects. For the jth cell, these are computed, respectively, by Eqs. (1)–(3) [32]:

$$U_j^m(z_j) = \frac{\mu_0 M_i V_i M_o V_o N}{4\pi}\left\{\frac{(z_j-\beta_j l_j)^2}{[(z_j-\beta_j l_j)^2+r_j^2]^{5/2}} - \frac{1}{[(z_j-\beta_j l_j)^2+r_j^2]^{3/2}}\right\} \tag{1}$$

$$U_j^s(z_j) = \frac{1}{2}k_j(z_j-l_j)^2 \tag{2}$$

$$U_j^g(z_j) = g m_j x_j \tag{3}$$

where $z_j = x_j - x_{j-1}$ is the relative motion between adjacent cell masses; $\mu_0 = 4\pi \times 10^{-7}$ H/m is permeability of free space; $M_{i,o} = 1.25 \times 10^6$ A/m are the magnetizations of the inner and outer magnets used in this study; $V_{i,o} = 3.62$ cm^3 are the volumes of the inner and outer magnets used in this study; r_j is the radius of the outer magnet circular array from the inner magnet center point, shown in Fig. 2(c); N is the number of radial array magnets ($N = 4$ in this research); m_j is the net mass of a cell; and g is gravitational acceleration. Note that by this notation, a minimum of two absolute mass displacements (x_j and x_{j-1}) are required to express the potential energy of each cell. Thus, an M-cell chain requires definition of $M + 1$ mass motions, although one cell could be a fixed, grounded coordinate. This feature is more plainly recognized by recalling that the *interface* between two cells induces bistability.

The total potential energy of an M-cell chain is the summation of the energy contributions for each cell with respect to mass displacement coordinates x_{1-M}. Fig. 3(a) plots the global minimum

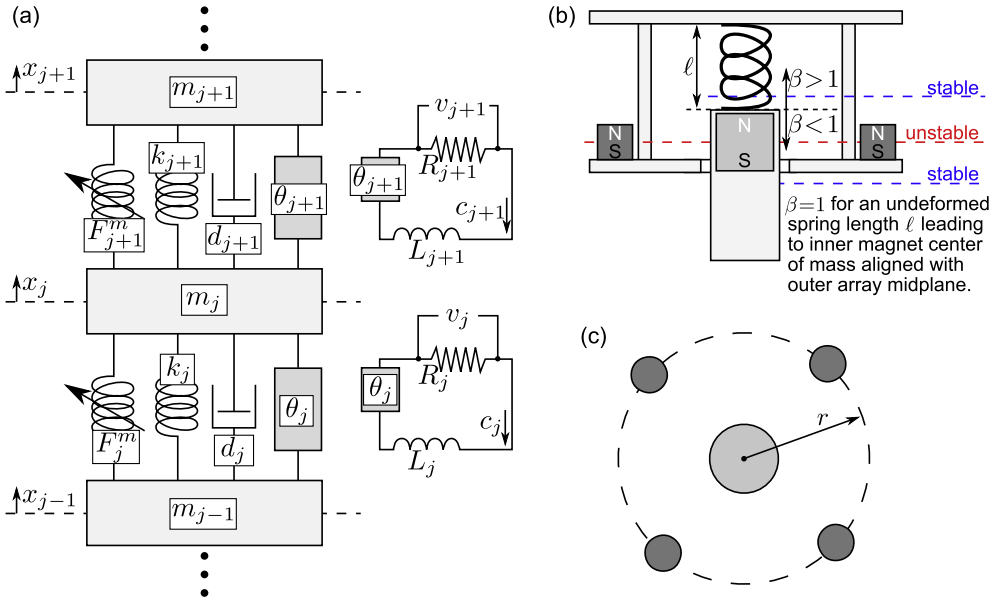

Fig. 2. (a) Schematic of the unit cell connected to nearest neighbor cells, and corresponding simplified energy storage circuitry. (b) Notational convention for spring undeformed length and scalar multiplier β. (c) Radial distance of outer magnet array to inner magnet center.

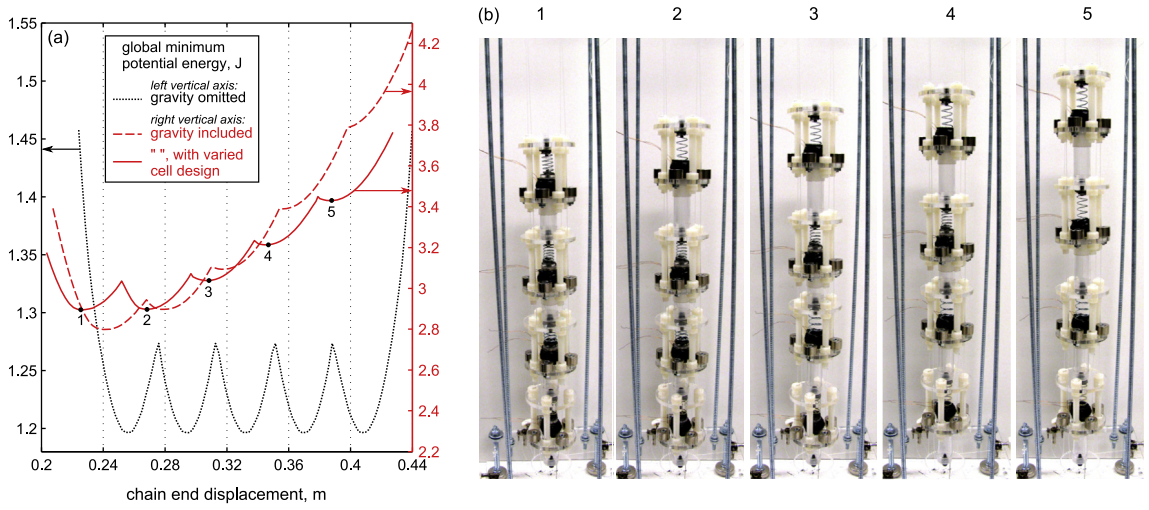

Fig. 3. (a) Global minimum potential energy profiles of 4-cell multistable chain as function of chain end displacement. (b) Stable configurations of the 4-cell chain with respect to their global minimum potential energies as labeled in (a) for solid red curve. (For interpretation of the references to colour in this figure legend, the reader is referred to the web version of this article.)

potential energy of a 4-cell multistable chain as a function of the chain end displacement, x_4. This is calculated by summing Eqs. (1)–(3) over the four mass displacements x_{1-4} and determining the minimum energy configuration for given x_4. A fixed base coordinate is included, $x_0 = 0$, representing an additional unmoving cell to which the first cell of coordinate x_1 is attached by spring and magnetic interfaces (e.g., the PTO system attached to the bottom of the WEC spar).

Fig. 3(a) shows that when neglecting gravity, the 4-cell chain composed of identical cells ($r_{1-4} = 26$ mm; $k_{1-4} = 770$ N/m; $\beta_{1-4} = 1$; $l_{1-4} = 83$ mm; $m_{1-4} = 264$ g) exhibits *five* configurations of stability as indicated by the five local minima (or wells) along the potential energy profile (black dotted curve). The energy required to extend the chain from one stable configuration to the next is given by the height of the energy barrier between wells, and is also related to the energy converted into electrical current following each impulsive drop into the adjacent well (i.e. to the next stable configuration). The same may be said of chain compression because the process is dynamically reversible.

However, for the PTO mechanism operating in a vertical axis of motion within the WEC spar, gravitational influences are not negligible. The red dashed curve of Fig. 3(a) shows the global minimum potential energy profile of a 4-cell chain having identical members when gravity is taken into consideration. The stabilities of the two most extended configurations are lost since they no longer exhibit local minima. This indicates that substantially reduced power is generated by extending and compressing the chain from lengths of approximately 0.37–0.41 m because impulsive transitions would not be induced. To remedy the concern of compromised stable configurations and recover favorable impulsive response energy conversion, it is necessary to vary cell design parameters along the chain length. Fig. 3(a) plots the global minimum potential energy profile of one such variable design by the red solid curve where the varied k_{1-4} and β_{1-4} values are

Table 1
Identified parameters from experimental system. Single entries refer to identical values for all cells of a multi-cell chain. Entries with multiple values $1-M$ represent values of a representative M-cell chain used in simulation and testing.

m_{1-4}, g 264	d_{1-4}, N s/m 11	k_{1-4}, N/m [770,718,612,612]
r_{1-4}, mm 26	l_{1-4}, mm 83	β_{1-4} [0.91,0.93,1,0.95]
L_{1-4}, mH [1.44,1.42,1.37,1.5]	R_{1-4}, Ω [12.4,10.7,12.4,13.4]	θ_{1-4}, N/A [0.65,0.67,0.73,0.71]

provided in Table 1 which are the experimental system parameters. Fig. 3(a) demonstrates that adjustment of varying cell design recovers stability of the most extended configurations which are now local minima around 0.35 and 0.39 m. Therefore, impulsive transitions between these stable states would again induce large flow of current via electromagnetic induction for improved energy conversion performance. Fig. 3(b) shows photographs of the experimental 4-cell multistable chain in the five stable configurations correspondingly labeled in 3(a).

As evident in Eqs. (1)–(3), several parameters may be adjusted to shape the global minimum potential energy profile for multi-cell chains having the same cell mass and magnet selections: the undeformed spring length l_j, the offset multiplier β_j, the spring constant k_j, and the outer magnet array radius r_j. Of these parameters, it is found that changing the array radius r_j may play the most dramatic role. Specifically, reducing r_j leads to greater barriers between stable configurations and, hence, greater energy converted to current flow following the impulsive transition. However, in the experimental system, the radial dimension was selected to be identical for all cells along the chain and adjustment of cell potential energies was only made by changing spring constant k_j and the undeformed spring length offset multiplier β_j, the latter being adjusted by modifying the frame structure heights. This decision was based on the exceptionally impulsive and energetic transitions amongst stable configurations that were observed in early prototype designs using radii $r_j < 26$ mm which led to failure of the epoxy joints connecting the springs to cell frame structures. Thus, although greater power was generated for cell designs using array radial dimensions $r_j < 26$ mm, practical considerations necessitated use of smaller energy barriers between stable configurations in the experimental system.

4. Multistable PTO chain dynamic modeling

A dynamic model of the multistable PTO chain is formulated to demonstrate its mode of power generation and to shed light on design factors critical to successful wave energy conversion. The forces on the jth cell mass are due to the four interface elements between adjacent cells, indicated in Fig. 2(a), as well as gravity. The interface force contributions between the jth and $(j-1)$th cells are given by Eqs. (4)–(7) using appropriate substitution for the relative coordinate $z_j = x_j - x_{j-1}$, while gravitational force on the jth cell is expressed by Eq. (8).

$$F_j^m(x_j - x_{j-1}) = -\frac{5\mu_0 M_i V_i M_o V_o N}{4\pi}\left\{\frac{x_j - x_{j-1} - \beta_j l_j}{\left[(x_j - x_{j-1} - \beta_j l_j)^2 + r_j^2\right]^{5/2}} - \frac{(x_j - x_{j-1} - \beta_j l_j)^3}{\left[(x_j - x_{j-1} - \beta_j l_j)^2 + r_j^2\right]^{7/2}}\right\} \tag{4}$$

$$F_j^s(x_j - x_{j-1}) = k_j(x_j - x_{j-1} - l_j) \tag{5}$$

$$F_j^d = d_j(\dot{x}_j - \dot{x}_{j-1}) \tag{6}$$

$$F_j^c = -\theta_j c_j \tag{7}$$

$$F_j^g = g m_j \tag{8}$$

The current induced to flow in the generically defined energy storage circuitry is c_j and the overdot operator $(\cdot)$ indicates differentiation with respect to time. The dynamic governing equations for the jth unit cell are derived:

$$m_j\ddot{x}_j + d_j(\dot{x}_j - \dot{x}_{j-1}) - d_{j+1}(\dot{x}_{j+1} - \dot{x}_j) + F_j^s(z_j) - F_{j+1}^s(z_{j+1}) + F_j^m(z_j) - F_{j+1}^m(z_{j+1}) + F_j^g - \theta_j c_j + \theta_{j+1} c_{j+1} = 0 \tag{9}$$

$$L_j\dot{c}_j + R_j c_j + \theta_j(\dot{x}_j - \dot{x}_{j-1}) = 0 \tag{10}$$

The coil inductance is L_j, and the load resistance of the circuitry is R_j. In experimentation this resistance is the sum of unit load and coil resistances. The voltage across the resistance is $v_j = R_j c_j$. Note that the *relative* velocities between the jth and $(j-1)$th cells induce flow of current and thus only one contributing term from corresponding mechanical responses appears in the electrical Eq. (10); this contrasts to the two electromagnetic forces working on the unit cell mass m_j motion due to induction of the jth and $(j+1)$th coils. The mechanical dissipations, here collectively given by constant d_j, are representative of losses in the linear spring deformations and losses from mass motions as they glide along the vertical guiding wires of the prototype. The guiding wires were taut, high-strength fishing lines which pass through small holes in the frame structures of the cells to constrain the motion of the chain to vertical, uni-axial motion. Sliding friction losses between the cells and the guiding wires were observed to be very small compared to dissipations related to the linear spring deformations.

The average power generated by an M-cell chain over a period of testing or simulation time τ is the sum of the time-averaged instantaneous electrical powers:

$$\widetilde{P} = \frac{1}{\tau}\sum_{j=1}^{M}\int v_j c_j dt \tag{11}$$

5. Extension–compression cycling

To validate the dynamic model, extension–compression cycles are prescribed as actuation upon the end link of an M-cell chain, which according to Fig. 1 may be rigidly connected to a moving WEC buoy. Cell 1 is connected to the fixed base through a bistable interface of linear spring and magnetic interactions. In all tests, the prototype system parameters are as provided in Table 1. Additionally, as identified from impulsive ring-down responses, the cells exhibited linear natural frequencies around 10 Hz and damping ratios around 0.16. This is in sharp contrast to previous directly driven PTO for mobile WEC that target natural frequencies closer to wave spectra, 0.1–1 Hz, and were critically damped [18]. Before experimentation, a check was made to ensure that the system was capable of supporting all 5 stable configurations exemplified in Fig. 3(b), i.e., that gravitational effects did not compromise stability. The check was likewise performed following experimentation to ensure that potential fatiguing influences had not compromised the 5 stable configurations; no such loss of stability was observed.

In absence of suitable laboratory actuators, the end cell of the chain was displaced by hand. Because sinusoidal displacements are more difficult to replicate by hand, the extension–compression cycles on the actuated end cell were triangular waves. The influences of triangular wave frequency and number of cells for the multistable PTO chain average power were evaluated for

experiments lasting 16 actuation cycles. To ensure that all transitions were triggered during each actuation cycle, the triangular wave peak-to-peak amplitude was approximately 1.2 times the maximum stroke of the stable configurations for the chain configuration under consideration. For [2–4]-cell chains, the strokes were [57.1,88.9,121] mm. Comparable simulations were performed by numerically integrating the governing equations of the *M*-cell chain using a fourth-order Runge–Kutta algorithm in MATLAB. Experimental data consisted of voltage measurements across the load resistances for each cell while simulated results included both electrical responses and cell mass locations. All tests and simulations began with the multistable chain compressed slightly more than the minimum stable configuration length, and the triangular wave excitation started from this bottom trough.

To demonstrate typical time responses from the series of tests and simulations, Fig. 4 presents two actuation periods of simulated (a,b) and measured (c) responses for a 4-cell chain undergoing extension–compression cycling at frequency 0.14 Hz. The positions of the cell masses are shown in Fig. 4(a); the triangular wave actuation trajectory on the 4th mass (chain end) is apparent.

As impulsive events are induced due to the sudden extension or compression of cell-to-cell interfaces from one stable position to the next, the cell mass displacements oscillate in underdamped ring-down behaviors. The greatest concentration of local vibration due to an impulse occurs between the two absolute mass displacements where the stability switch occurred. Thus, since the *relative* velocity between these two masses is related to the flow of current in the external circuitry, Fig. 4(b) shows that an impulsive spike of voltage is induced across the load resistance connected to the coil interfacing these two cells.

As exemplified by the close-up insets in Fig. 4(a), the first impulsive transition to occur is a sudden increase in distance between the chain end (4th cell) and cell 3 mass. The close-up inset in Fig. 4(b) shows that this response induces greatest impulsive voltage response across the load connected to the coil positioned between cell 3 and the chain end. The transmission of this vibration to adjacent members in the chain induces additional small electrical impulses, although in this example stability transitions are not simultaneously triggered between those cells. The next stability transition occurs between cells 1 and 2 and therefore greatest voltage is induced between cells 1 and 2. Similar trends are observed throughout the actuation cycles: progressive ring-down responses due to the impulsive switches, high electrical output in circuitry connected to the coil interfacing the adjacent cells that underwent stability transition, and transmission of ring-down dynamics along the chain to enhance overall energy conversion.

Good agreement is found comparing simulated and experimental electrical responses Fig. 4(b and c), respectively. The average power over 16 cycles of this example were likewise in good agreement: 17.1 mW in simulation to 16.9 mW in experiment. While this is below the ultimate aim of 1–10 W for powering sea-borne instrumentation or communication equipment, these results represent early efforts at developing a new PTO methodology without attempts towards design optimization. Additionally, recalling remarks in Section 2, it was found from additional experimental efforts that the voltage impulses were capable of peaking near 10 V but this required designs that led to early failure of the epoxy joints securing the springs to the frame structures. In light of these factors, with continued development of the multistable PTO chain it is anticipated that the average powers may approach the target goals.

Overall, the underdamped impulsive dynamics of the multistable PTO chain are in great contrast to directly driven PTO mechanisms that employ highly damped oscillations at frequencies concurrent with the peak wave spectral density. Instead of matching a PTO characteristic frequency to the actuating wave motion, the proposed PTO *transforms* the input motions to higher frequency dynamics for energy conversion. By gliding along low friction wires and exhibiting underdamping dynamics, the PTO chain ensures power generation so long as impulsive events are induced.

6. Influences of chain modularity and actuation frequency: experimental and numerical comparison

Fig. 5(a) presents the computed average powers for all cases of actuation frequency and chain cell number; measured results are filled data points while predicted values are unfilled data points. The actuation frequency of a given example is represented in Fig. 5(b) by the corresponding data point shape as utilized in Fig. 5(a). For example, a 2-cell chain was tested and modeled for excitation frequency near 0.58 Hz, see Fig. 5(b), and measured and predicted results closely agree regarding average power generation around 30 mW, see Fig. 5(a).

Overall, there is good agreement between simulated and experimental results of average power although the model tends to underestimate power generation as both the number of chain cells and excitation frequency increase. The discrepancy may be due to greater difficulty in controlling the experimental actuating waveform by hand for multi-cell chains as the excitation frequency increases because rapidly occurring impulsive dynamics exert large forces on the actuated end cell. Nevertheless, the good agreement between predictions and measurements provides confidence

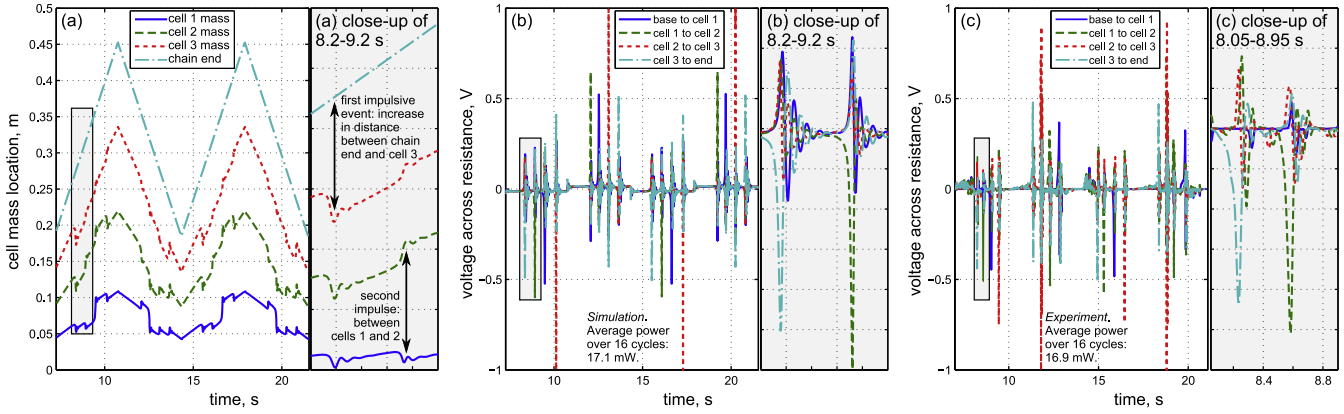

Fig. 4. Extension–compression cycling of 4-cell multistable chain. (a) Simulated cell mass locations. (b) Simulated voltages across resistances. (c) Experimental voltage measurements.

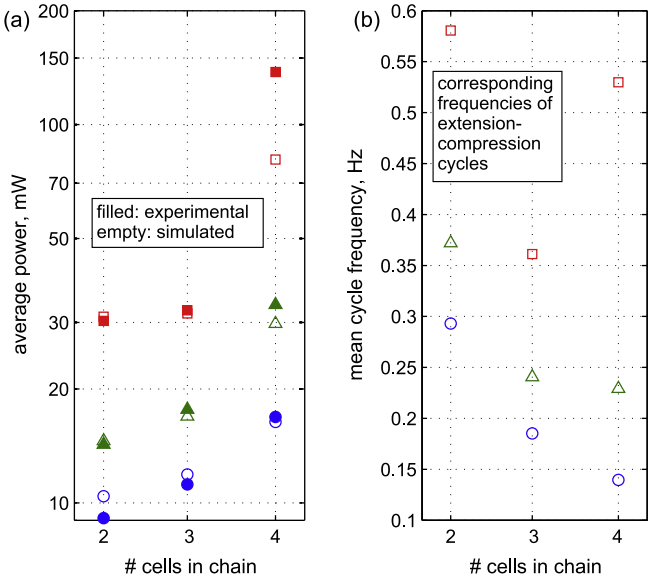

Fig. 5. Extension–compression testing results. (a) Average powers for *M*-cell multistable chains when actuated at various triangular wave frequencies. (b) Mean excitation frequency of the experiment and simulation, denoted by the same data point shape as average power results given in (a).

in the model to explore design dependencies that cannot be as easily investigated by the prototype. Some specific findings from Fig. 5 are first worth highlighting. It is seen that as cells are added to the chain, greater power is generated despite testing at lower frequencies. For example, considering the triangle data points, increasing the number of chain cells from 2 to 4 is predicted and measured to increase average power from approximately 14–30 mW even though the actuation frequency decreases from 0.37 to 0.22 Hz. Thus power increases by >100% at the same time the excitation slows down by 40%. In this manner, increased modularity of the chain retains high energy conversion capability while concurrently improving power generation at lower frequencies more representative of typical wave spectra.

7. Numerical investigation of influences on specific power

Having validated the model over a large range of design and excitation cases, Fig. 6 presents simulated results of energy conversion performance for actuation at a given frequency but for increasing numbers of cells in the multistable chain. As before, the triangular wave excitation peak-to-peak amplitude was approximately 1.2 times the stable configuration stroke of the *M*-cell chain. The frequencies span 0.1–0.7 Hz in 0.05 Hz increments and simulations were conducted lasting 40 excitation cycles. Lines connecting data points in Fig. 6 are provided to assist in visualizing the main trends. In Fig. 6 average *specific power* is presented, that is the ratio of average power to *M*-cell chain mass, to provide a more meaningful performance metric.

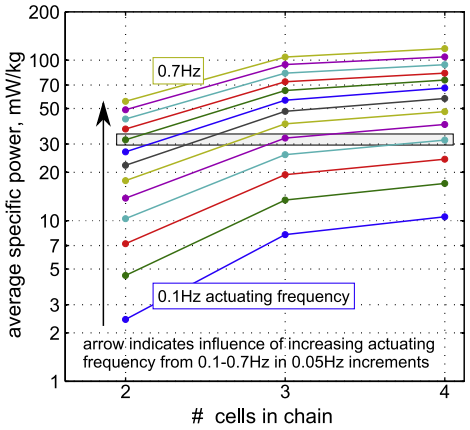

Fig. 6. Average specific power for *M*-cell chains as actuation frequency increases from 0.1 to 0.7 Hz in 0.05 Hz increments.

Fig. 6 plainly demonstrates the trend suggested in Fig. 5 that increased excitation frequency yields higher levels of average power. However, the plot reveals that as frequency increases the power generation appears to gradually saturate towards an upper limit, albeit on a *logarithmic* scale. In evaluating the time series of such simulations (not shown here), the saturation corresponds to impulse transitions occurring almost continuously along the chain. This is intuitively the desired approach to achieve maximum energy conversion performance because it minimizes time elapsed between impulsive kinetics. Fig. 6 also demonstrates that increased number of cells can yield dramatic improvement in specific power. For example, at 0.1 Hz actuation frequency, *doubling* the number of cells from 2 to 4 leads to *more than four* times increase in specific power: 2.43–10.6 mW/kg. This exemplifies that transmission of impulsive bistable dynamics along multi-cell chains helps to more readily convert the kinetic motions to electrical energy, thus yielding a more potent PTO for the same wave excitation. Finally, Fig. 6 further supports the observation from experimental and simulated results of Fig. 5 that increased modularity empowers similar or improved performance when actuated at lower frequencies. The shaded region in Fig. 6 shows that increased number of links in the chain yields approximately the same power while dramatically lowering the operating frequency: 31.8 mW/kg for 2-cell at 0.5 Hz; 32.7 mW/kg for 3-cell at 0.3 Hz; and 31.7 mW/kg for 4-cell at 0.25 Hz.

8. PTO performance under wave excitation

Lastly, study of chain responses due to characteristic wave actuation is important to evaluate viability of the proposed PTO mechanism and uncover design factors critical to power generation. Wave heave actuating motions are simulated using a Fourier series expansion of water surface elevation [18,19]. A significant wave amplitude of 0.025 m is set for a wave spectrum collected by the National Data Buoy Center [33]. The wave spectral data was acquired during the month of September 2011 as measured by buoy #46015 which is located approximately 25 km from the west coast of Oregon, USA. The simulation used the resulting Fourier expansion of water surface elevation as the actuating displacement on the end of the 4-cell multistable chain.

Fig. 7(a and b) shows the cell mass displacements and voltages, respectively, in response to the wave input. Several aspects of Fig. 7 are specifically informative as relate to design guidelines. The first is the detriment to performance due to low excitation levels (too small chain end displacements), since in some cases throughout the time series, several seconds elapse without inducement of an impulsive event. To sustain more frequent impulse triggering as actuation amplitudes decrease, according to Section 3 and Fig. 3 one resolution is to reduce the distance between stable positions. This means the chain stable configurations would be closer to each other and thus less actuating displacement would be required to cross from one stable state to the next, exciting the impulse. For the present prototype design, one way to accomplish this is by reducing the outer magnet array radius, all other parameters remaining the same.

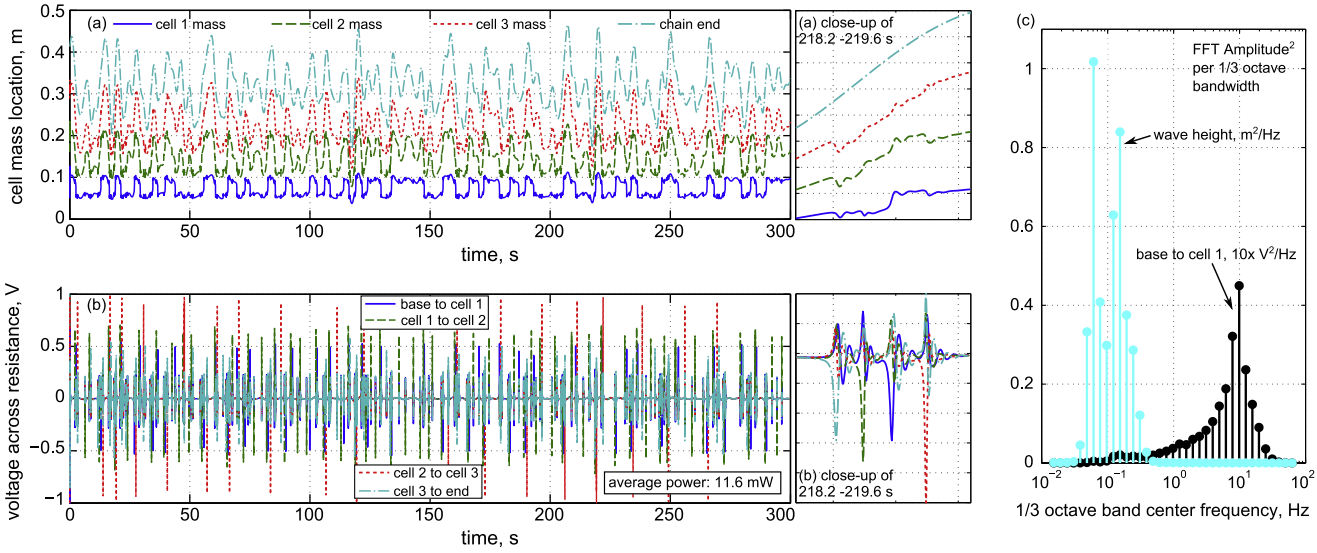

Fig. 7. Simulated response of 4-cell multistable PTO chain mechanism due to wave excitation. (a) Cell mass displacements and (b) voltages across resistances. (c) FFT spectra averaged over 1/3 octave bands of the base to cell 1 voltage and the wave height, demonstrating that the PTO chain transforms lower frequency actuating motions to higher frequency oscillations for energy conversion.

The second important element of Fig. 7 is that fast extension or compression of the chain leads to near continuous triggering of impulsive switches along the chain, e.g. as shown in the close-up views in Fig. 7(a and b). It is seen that the 4 successive voltage spikes occur rapidly enough such that the ring-down responses do not fully decay from one spike to the next. This explains the result in Fig. 6 that showed higher actuation frequencies – comparable to fast changes in wave height in Fig. 7(a) – led to an apparent saturation of power generation. Fig. 7(b) shows that performance saturation is likely due to insufficient time elapsed between individual impulse events to fully convert the kinetic energy in the electrical circuitry.

Finally, Fig. 7(c) plots the FFT spectra of wave height and the base-to-cell 1 voltage as computed over the full time series and averaged across 1/3 octave bands. Fig. 7(c) exemplifies the essential nature of frequency transformation by which the PTO chain transforms low frequency wave inputs into higher frequency dynamics for energy conversion. It is apparent that the wave spectrum is concentrated around 0.1 Hz, whereas the voltage between the base and cell 1 occurs primarily at frequencies around 10 Hz, corresponding to the identified natural frequencies of the cells. The transformation of the actuation spectra by two orders of magnitude for energy conversion represents the robust power generation principle of the multistable chain. Because impulsive events are able to be induced for *any* actuating frequency so long as actuating displacements are at least the distance between two stable configurations, favorable energy conversion may be ensured.

9. Conclusion

To successfully realize mobile WEC architectures useful in a wide range of exciting sea states, this research developed a new PTO mechanism that is less susceptible to the limitations of direct drive PTO by integrating two recent vibration energy harvesting concepts: *bistable impulsive* interactions for converting low frequency input motions to higher frequency energy harvesting dynamics, and enhanced performance using *coupled system* architectures. Assessment of the global minimum potential energy profile of the multistable PTO chain defines the minimum actuation displacements and energies required to induce impulsive kinetics for power generation and guides system design based upon anticipated actuating wave motions. Using an experimentally validated model, the influences of number of chain cells and actuation frequency on the resulting energy conversion performance indicate that modularity of the chain may greatly improve net power generation by transmitting local impulses along the chain. Energy conversion performance due to modeled wave actuations and controlled excitations both suggest that rapid, successive inducement of impulsive kinetics along the chain is the most favorable for energy conversion. Because impulse generation is governed by the designed distance between stable configurations with respect to expected wave excitations, this finding provides a pathway to ensure effective energy conversion is maintained.

Acknowledgements

This research was supported in part by the University of Michigan Summer Research Opportunity Program, the University of Michigan Undergraduate Research Opportunity Program, and the University of Michigan Collegiate Professorship fund.

References

[1] Falnes J. A review of wave-energy extraction. Mar Struct 2007;20:185–201.
[2] Drew B, Plummer AR, Sahinkaya MN. A review of wave energy converter technology. Proc Inst Mech Eng, Part A: J Power Energy 2009;223:887–902.
[3] Falcão AF de O. Wave energy utilization: a review of the technologies. Renew Sustain Energy Rev 2010;14:899–918.
[4] Scruggs J, Jacob P. Harvesting ocean wave energy. Science 2009;323:1176–8.
[5] Chiba S, Waki M, Wada T, Hirakawa Y, Masuda K, Ikoma T. Consistent ocean wave energy harvesting using electroactive polymer (dielectric elastomer) artificial muscle generators. Appl Energy 2013;104:497–502.
[6] He F, Huang Z, Law AWK. An experimental study of a floating breakwater with asymmetric pneumatic chambers for wave energy extraction. Appl Energy 2013;106:222–31.
[7] Rhinefrank K, Schacher A, Prudell J, Brekken TKA, Stillinger C, Yen JZ, et al. Comparison of direct-drive power takeoff systems for ocean wave energy applications. IEEE J Oceanic Eng 2012;37:35–44.
[8] Delli Colli V, Cancelliere P, Marignetti F, Di Stefano R, Scarano M. A tubular-generator drive for wave energy conversion. IEEE Trans Ind Electron 2006;53:1152–9.
[9] Danielsson O, Eriksson M, Leijon M. Study of a longitudinal flux permanent magnet linear generator for wave energy converters. Int J Energy Res 2006;30:1130–45.
[10] Waters R, Stålberg M, Danielsson O, Svensson O, Gustafsson S, Strömstedt E, et al. Experimental results from sea trials of an offshore wave energy system. Appl Phys Lett 2007;90:034105.

[11] Mueller MA, Polinder H, Baker N. Current and novel electrical generator technology for wave energy converters. In: Proceedings of the electric machines and drives conference, 2007, IEMDC '07. Antalya, Turkey; 2007. p. 1401–6.
[12] Rhinefrank K, Agamloh EB, von Jouanne A, Wallace AK, Prudell J, Kimble K, et al. Novel ocean energy permanent magnet linear generator buoy. Renew Energy 2006;31:1279–98.
[13] Prudell J, Stoddard M, Amon E, Brekken TKA, von Jouanne A. A permanent-magnet tubular linear generator for ocean wave energy conversion. IEEE Trans Ind Appl 2010;46:2392–400.
[14] Huang SR, Chen HT, Chung CH, Chu CY, Li GC, Wu CC. Multivariable direct-drive linear generators for wave energy. Appl Energy 2012;100:112–7.
[15] Davis EP, Ertekin RC, Riggs HR. A buoy-based WEC device to provide low power to sensors. In: Proceedings of the ASME 2009 28th international conference on ocean, offshore and arctic engineering. Honolulu, Hawaii, USA. OMAE2009-80091; 2009.
[16] Nolte J, Ertekin RC, Davis EP. In-ocean experiments of a wave energy conversion device when moored to an anchor and to a drogue. J Ocean Technol 2013;8:72–85.
[17] Symonds D, Davis E, Ertekin RC. Low-power autonomous wave energy capture device for remote sensing and communications applications. In: Proceedings of IEEE energy conversion congress and exposition. Atlanta, Georgia, USA; 2010. p. 2392–6.
[18] Grilli AR, Merrill J, Grilli ST, Spaulding ML, Cheung JT. Experimental and numerical study of spar buoy-magnet/spring oscillators used as wave energy absorbers. In: Proceedings of the seventeenth (2007) international offshore and polar engineering conference. Lisbon, Portugal; 2007. p. 489–96.
[19] Bastien SP, Sepe RB, Grilli AR, Grilli ST, Spaulding ML. Ocean wave energy harvesting buoy for sensors. In: Proceedings of the energy conversion congress and exposition, ECCE 2009. San Jose, CA, USA; 2009. p. 3718–25.
[20] Grilli ST, Grilli AR, Bastien SP, Sepe Jr RB, Spaulding ML. Small buoys for energy harvesting: experimental and numerical modeling studies. In: Proceedings of the twenty-first (2011) international offshore and polar engineering conference. Maui, Hawaii, USA; 2011. p. 598–05.
[21] Gemme DA, Bastien SP, Sepe Jr RB, Montgomery J, Grilli ST, Grilli AR. Experimental testing and model validation for ocean wave energy harvesting buoys. In: Proceedings of the IEEE energy conversion congress and exposition, ECCE13. Denver, CO, USA; 2013. p. 1407.
[22] Glendenning I. Ocean wave power. Appl Energy 1977;3:197–222.
[23] Brekken TKA, Hapke HM, Stillinger C, Prudell J. Machines and drives comparison for low-power renewable energy and oscillating applications. IEEE Trans Energy Convers 2010;25:1162–70.
[24] Wickenheiser AM, Garcia E. Broadband vibration-based energy harvesting improvement through frequency up-conversion by magnetic excitation. Smart Mater Struct 2010;19:065020.
[25] Jung SM, Yun KS. Energy-harvesting device with mechanical frequency-up conversion for increased power efficiency and wideband operation. Appl Phys Lett 2010;96:111906.
[26] Tang L, Yang Y, Soh CK. Improving functionality of vibration energy harvesters using magnets. J Intell Mater Syst Struct 2012;23:1433–49.
[27] Karami MA, Farmer JR, Inman DJ. Parametrically excited nonlinear piezoelectric compact wind turbine. Renew Energy 2013;50:977–87.
[28] Harne RL, Wang KW. A review of the recent research on vibration energy harvesting via bistable systems. Smart Mater Struct 2013;22:023001.
[29] Pellegrini SP, Tolou N, Schenk M, Herder JL. Bistable vibration energy harvesters: a review. J Intell Mater Syst Struct 2013;24:1303–12.
[30] Harne RL, Thota M, Wang KW. Bistable energy harvesting enhancement with an auxiliary linear oscillator. Smart Mater Struct 2013;22:125028.
[31] Wu Z, Harne RL, Wang KW. Energy harvester synthesis via coupled linear-bistable system with multistable dynamics. ASME J Appl Mech 2014;81:061005.
[32] Mann BP, Owens BA. Investigations of a nonlinear energy harvester with a bistable potential well. J Sound Vib 2010;329:1215–26.
[33] National Data Buoy Center. <http://www.ndbc.noaa.gov/>.